

## PAPER

Cite this: *RSC Adv.*, 2016, 6, 16608

# A targeted agent with intercalation structure for cancer near-infrared imaging and photothermal therapy†

 Chunyang Li,<sup>a</sup> Ruizheng Liang,<sup>\*a</sup> Rui Tian,<sup>a</sup> Shanyue Guan,<sup>a</sup> Dongpeng Yan,<sup>a</sup> Jiaoyang Luo,<sup>\*b</sup> Min Wei,<sup>\*a</sup> David G. Evans<sup>a</sup> and Xue Duan<sup>a</sup>

A new targeted photothermal agent used in cancer photothermal therapy (PTT) is synthesized by co-intercalation of indocyanine green (ICG) and targeting folic acid (FA) into the interlamellar gallery of layered double hydroxide (LDH). The resulting composite material (ICG-FA/LDH) possesses an interlayer distance of 2.503 nm, and a uniform particle size with an equivalent hydrodynamic diameter of 127 nm. ICG presents a monomeric state in the LDH gallery, owing to the supermolecular interactions between the LDH host and ICG guest, which results in a largely-enhanced photothermal conversion efficiency. *In vitro* tests performed with KB cells demonstrate a highly enhanced cellular uptake and excellent imaging ability for the ICG-FA/LDH. The photothermal conversion studies show that an ultra-low dosage of ICG-FA/LDH (equivalent ICG 10  $\mu\text{g mL}^{-1}$ ) under weak near-infrared (NIR) irradiation (8 min; 1.1  $\text{W cm}^{-2}$ ) achieves a significant temperature increase from 19.8 °C to 51.0 °C. Therefore, a satisfactory *in vitro* PTT effectiveness of the ICG-FA/LDH composite is obtained, and it exhibits cellular damage as high as 87.4% with an ultra-low dosage of ICG (8  $\mu\text{g mL}^{-1}$ ) and weak NIR irradiation (1.1  $\text{W cm}^{-2}$ , 12 min). In addition, the photothermal agent ICG-FA/LDH displays good targeting capability, biocompatibility and low cytotoxicity. It is expected that the unique ICG-FA/LDH with integrated fluorescence imaging and photothermal therapy can be potentially used in the cell labeling and PTT area.

 Received 10th November 2015  
 Accepted 15th January 2016

DOI: 10.1039/c5ra23686j

www.rsc.org/advances

## 1. Introduction

Photothermal therapy (PTT) as a promising cancer therapeutic method, which involves the employment of near-infrared (NIR) absorbing agents to convert light to heat giving rise to the death of cancer cells,<sup>1–3</sup> has attracted tremendous attention in recent years. PTT is a non-invasive and controllable modality with minimal side effects, which has shown excellent therapeutic effects in many reports.<sup>4–6</sup> Although a variety of inorganic nanomaterials (*e.g.*, gold, carbon and copper nanoparticles) are explored as photothermal agents,<sup>7–14</sup> they generally suffer from long term safety problems (*e.g.*, high toxicity and inferior metabolizability) which limit their further applications.<sup>15,16</sup>

In comparison, organic photothermal agents, due to their good biocompatibility and biodegradability, can serve as a promising candidate in PTT. Common organic photothermal

agents include indocyanine green (ICG),<sup>17–19</sup> polypyrrole,<sup>20–22</sup> polythiophene,<sup>23,24</sup> dopamine<sup>25,26</sup> and so on. In particular, ICG shows superior performances with high photothermal conversion efficiency and photoacoustic/photodynamic response;<sup>27,28</sup> moreover, the use of ICG in fluorescence imaging has been widely studied owing to its excellent property of NIR fluorescence.<sup>29–31</sup> However, the high photo-thermal conversion efficiency of ICG is far from fully demonstrated, as a result of drawbacks including a short half-life and fast degradation in aqueous solution.<sup>32,33</sup> Furthermore, the non-specific binding of proteins toward ICG is rather undesirable for drug accumulation at tumor sites.<sup>34–36</sup> In order to overcome these limitations, a range of carriers have been studied (*e.g.*, polymers, liposomes and proteins),<sup>35,37,38</sup> but several issues (*e.g.*, structure controllability and stability) are not well-resolved. Therefore, the development of new photothermal agents with facile preparation, targeting capability and superior PTT performances, remains a challenging goal.

Layered double hydroxides (LDHs) are a typical class of layered materials represented by the general formula  $[\text{M}^{2+}_{1-x}\text{M}^{3+}_x(\text{OH})_2](\text{A}^{n-})_{x/n} \cdot m\text{H}_2\text{O}$ , in which  $\text{M}^{2+}$  and  $\text{M}^{3+}$  are divalent and trivalent cations respectively, and  $\text{A}^{n-}$  is the charge-balancing and exchangeable interlayer anion.<sup>39–41</sup> It has been reported that the dispersity and stability of organic molecules can be highly improved after their intercalation into

<sup>a</sup>State Key Laboratory of Chemical Resource Engineering, Beijing University of Chemical Technology, Beijing 100029, P. R. China. E-mail: liangruizheng2000@163.com; weimin@mail.buct.edu.cn; Fax: +86-10-6442-5385

<sup>b</sup>Institute of Medicinal Plant Development, Chinese Academy of Medical Sciences & Peking Union Medical College, Beijing 100193, P. R. China. E-mail: luojiaoyang1986@163.com

† Electronic supplementary information (ESI) available. See DOI: 10.1039/c5ra23686j

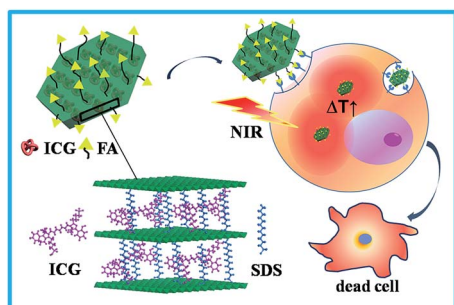
LDH interlamellar gallery.<sup>42–44</sup> Moreover, LDHs have also been investigated as drug nanocarriers due to their low toxicity, enhanced cellular uptake and good biodegradation.<sup>45–47</sup> This motivates us to co-intercalate photothermal molecule (indocyanine green, ICG) and targeting agent (folic acid, FA) into the interlayer of LDH, so as to obtain a new targeted photothermal agent used in PTT, which would exhibit the following advantages: (i) the host–guest interactions would improve the stability of ICG, extend half-life period and thus increase the efficiency of photo-thermal transformation; (ii) the organic–inorganic composite structure promotes the hydrophilicity and biocompatibility of ICG, leading to an enhancement in drug permeability/retention. In addition, the over-expression of FA toward cancer cells would increase the drug uptake, showing a good targeting performance.

In this work, a targeted photothermal agent (ICG–FA/LDH) was synthesized by co-intercalation of ICG and FA into the LDH gallery, which shows an excellent near-infrared (NIR) imaging and superior photothermal therapy effect. XRD and FT-IR spectra confirm the co-existence of ICG and FA molecule in the interlayer region of LDH matrix; UV-vis-NIR spectroscopy proves the monomer state of ICG, which is a key factor for its photothermal conversion efficiency. Both a satisfactory NIR imaging and PTT effectiveness are demonstrated for the ICG–FA/LDH photothermal agent over *in vitro* tests performed with KB cells, with a cellular damage as high as 87.4% (ICG: 8  $\mu\text{g mL}^{-1}$ ; NIR irradiation energy: 1.1  $\text{W cm}^{-2}$ , 12 min). The host–guest interaction inhibits the aggregation of ICG and enhances its photo-thermal transformation in the LDH gallery; the suitable particle size and biocompatibility of the ICG–FA/LDH composite facilitate the drug delivery, accounting for the excellent PTT performances. In particular, the incorporation of FA endows ICG–FA/LDH with a targeting capability, which would be favor of its further application.

## 2. Results and discussion

### 2.1 Structural and morphological characterization

ICG, FA and sodium dodecyl sulfonate (SDS) were co-intercalated into the interlayer region of LDH by the coprecipitation method, in which SDS serves as a dispersant for improving the dispersibility of ICG. Scheme 1 illustrates the



**Scheme 1** Schematic illustration of the ICG–FA/LDH structure and the process of photothermal therapy.

structure of ICG–FA/LDH and the process of photothermal therapy. Since the loading density of ICG in the LDH interlamination (denoted as ICG(*x*%)/LDH) directly determines its aggregation state and the resulting photothermal conversion efficiency, this parameter was firstly investigated.

As shown in Fig. 1a, the powder XRD patterns of ICG(*x*%)/LDH samples (*x*% ranges in 1–10%) exhibit a series of narrow and strong (00*l*) reflections, indicating the formation of LDH structure with an interlayer distance of  $\sim 2.516$  nm. The co-intercalation of ICG and SDS was further confirmed by the FT-IR spectra (Fig. S1†). The characteristic absorption peaks at 2923 and 2847  $\text{cm}^{-1}$  are assigned to the asymmetric  $\nu_{\text{as}}(\text{CH}_2)$  and symmetric  $\nu_{\text{s}}(\text{CH}_2)$  vibration of SDS while the peaks at 900–650  $\text{cm}^{-1}$  correspond to the vibration of  $\delta(\text{Ar-H})$  of ICG. The chemical compositions of these samples measured by inductively coupled plasma atomic emission spectroscopy (ICP-AES) and elemental analysis are listed in Table S1.† We also performed the TGA measurement of ICG(2%)/LDH (see Fig. S2† and corresponding discussion), and the result accords with the elemental analysis. Fig. S3† shows SEM images and particle size distribution of ICG(*x*%)/LDH samples. The ICG(1%)/LDH and ICG(2%)/LDH display a regular platelet morphology with hydrodynamic diameter of 56 nm and 116 nm, respectively. However, with the increase of ICG loading from 3% to 10%, serious aggregation with large particle size (above 300 nm) is observed. Thus, from the viewpoint of hydrodynamic diameter for cell uptake, an ICG loading of 2% is chosen for further study.

The targeting agent FA was subsequently introduced to prepare the ICG–FA/LDH composite material. As shown in Fig. 1a, the ICG(2%)–FA(20%)/LDH sample exhibits a rather similar XRD pattern to ICG(2%)/LDH, with  $d_{003}$  basal spacing of 2.503 nm. The FT-IR spectra (Fig. 1b) verify the coexistence of FA: compared with ICG(2%)/LDH, additional absorption bands at 1607  $\text{cm}^{-1}$  and 1401  $\text{cm}^{-1}$  are observed, which are assigned to the symmetrical  $\nu_{\text{s}}(\text{C=O})$  and asymmetric  $\nu_{\text{as}}(\text{C=O})$  vibration of FA. SEM image (Fig. 1c) shows that the sample of

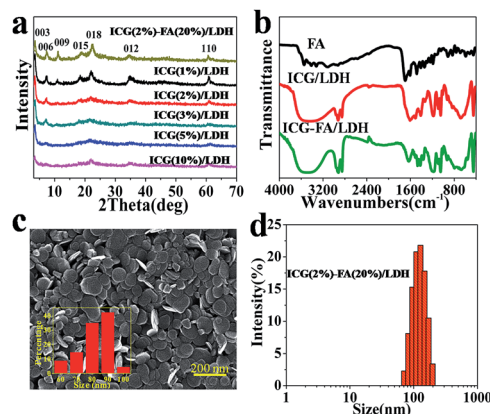


**Fig. 1** (a) XRD patterns of various ICG(*x*%)/LDH composites with *x*% ranging from 1% to 10% and the sample of ICG(2%)–FA(20%)/LDH. (b) FT-IR spectra of FA, ICG(2%)/LDH and ICG(2%)–FA(20%)/LDH. (c) SEM image of the ICG(2%)–FA(20%)/LDH sample with particle size distribution shown in the inset. (d) Particle size distribution of ICG(2%)–FA(20%)/LDH determined by dynamic lighting scattering (DLS).

ICG(2%)-FA(20%)/LDH possesses a uniform plate-like morphology with particle size ranging in 60–100 nm. Moreover, its equivalent hydrodynamic diameter in aqueous solution was determined to be  $\sim 127$  nm (Fig. 1d). The zeta potential of ICG(2%)/LDH is 34 mV; while it changes to  $-9$  mV for the sample of ICG(2%)-FA(20%)/LDH (Fig. S4<sup>†</sup>), indicating the co-loading of FA.

ICG tends to dissolve in methanol with two UV-vis-NIR absorbance regions (Fig. 2a): the peak centered at 784 nm is attributed to the monomer absorption; while the one at 718 nm corresponds to the J-aggregates (dimers or multimers) due to the van der Waals forces and hydrophobic interactions between ICG molecules.<sup>48–50</sup> For the samples of ICG(2%)/LDH and ICG(2%)-FA(20%)/LDH, a significant red-shift is observed. For instance, the monomer absorption peak moves to 816 nm and 833 nm, respectively, which can be attributed to the variation in polarity of microenvironment between ICG in LDH gallery and in methanol. Furthermore, additional absorption peaks at 290 nm and 310 nm assigned to FA are observed in the case of ICG(2%)-FA(20%)/LDH sample, indicating the incorporation of FA. Subsequently, the influence of ICG loading on its state was studied for ICG(x%)/LDH samples (Fig. 2b: x% ranges in 1%–10%). A relative ratio between monomer and aggregate ( $I_{\text{monomer}}/I_{\text{aggregate}}$ ) was calculated by the respective absorption intensity (inset of Fig. 2b), from which this ratio increases first and then decreases along with the enhancement of ICG loading from 1% to 10%. The sample of ICG(2%)/LDH possesses the largest value, which indicates the best monodispersity of ICG in this sample.

ICG is extremely unstable in the environment and easy to lose its photothermal conversion activity as a result of structural decomposition, thus the stability of ICG is a crucial factor for its practical application. In order to investigate the long-term

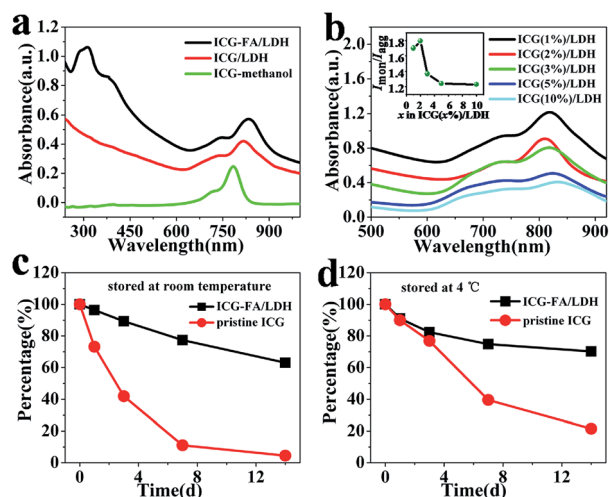


Fig. 2 (a) UV-vis-NIR absorption spectra of pristine ICG in methanol, ICG(2%)/LDH and ICG(2%)-FA(20%)/LDH in aqueous solution; (b) UV-vis-NIR absorption spectra of ICG(x%)/LDH composites with x% ranging in 1–10% (ICG concentration in solution:  $10 \mu\text{g mL}^{-1}$ ); the inset shows the ratio of  $I_{\text{monomer}}/I_{\text{aggregate}}$  as a function of x%. (c) and (d) The stability measurements over pristine ICG and ICG(2%)-FA(20%)/LDH stored at room temperature and 4 °C, respectively.

performance, the stability of pristine ICG and ICG(2%)-FA(20%)/LDH was measured by UV-vis-NIR absorption spectroscopy without light exposure (Fig. 2c, d and S5<sup>†</sup>). The pristine ICG in aqueous solution presents a poor stability stored at room temperature, with a fast decline of 94% in monomer absorption after 14 days. Even at the temperature of 4 °C, a loss of 78.6% is found. In contrast, for the sample of ICG(2%)-FA(20%)/LDH, a marked enhancement in storage stability is demonstrated: 62.3% of monomer absorption intensity is maintained at room temperature, and this value even increases to 70.1% at 4 °C. Therefore, the intercalation of ICG into the LDH gallery can improve its stability to a large extent, which is in favor of storage and further clinical application.

The photothermal conversion efficiency of ICG(x%)/LDH and ICG(2%)-FA(20%)/LDH was further investigated, which is the key factor for PTT performance. The photothermal conversion efficiency was evaluated over LDH, pristine ICG, ICG(x%)/LDH and ICG(2%)-FA(20%)/LDH samples (ICG concentration in solution:  $10 \mu\text{g mL}^{-1}$ ), by plotting the sample temperature as a function of NIR laser irradiation time (Fig. 3a). No obvious temperature change is observed for pure water upon irradiation; while LDH only promotes a slight temperature increase. The presence of pristine ICG distinctly accelerates this process, and the temperature rises to 42.0 °C after 480 s irradiation, indicating its good photothermal conversion ability. In the case of ICG(x%)/LDH samples, the photothermal conversion efficiency increases at first (from 1% to 2%) to a maximum; the ICG(2%)/LDH sample shows the highest photothermal conversion efficiency: a NIR irradiation for 480 s results in a temperature increase from 19.8 °C to 52.2 °C. For the pristine ICG sample, its aggregation state occurs due to the strong  $\pi$ - $\pi$  interaction, and a part of energy produced from the light-to-thermal transformation is consumed to conquer the resistance of molecular vibration. However, in the case of ICG/LDH sample, the host-guest interactions between LDH and ICG obviously restrain the aggregation of ICG, which decreases this energy consumption and thus enhances the light-to-thermal energy transformation. However, the photothermal conversion efficiency decreases along with a further enhancement of ICG loading (from 2% to 10%); the sample of ICG(10%)/LDH even declines

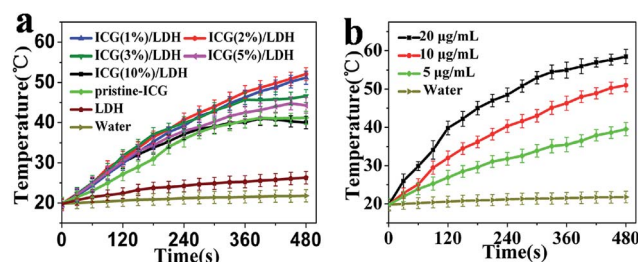


Fig. 3 Temperature increase as a function of NIR laser irradiation time (wavelength: 808 nm; power density:  $1.1 \text{ W cm}^{-2}$ ) over various samples: (a) LDH, pristine ICG and ICG(x%)/LDH samples (ICG concentration in solution:  $10 \mu\text{g mL}^{-1}$ ); (b) the sample of ICG(2%)-FA(20%)/LDH with different ICG concentration ( $5$ – $20 \mu\text{g mL}^{-1}$ ) in solution.

to the same level of pristine ICG. This result agrees well with the highest  $I_{\text{monomer}}/I_{\text{aggregate}}$  ratio in ICG(2%)/LDH (Fig. 2b). In addition, compared with pristine ICG, ICG(2%)/LDH shows a maintenance of increased temperature while pristine ICG displays an obvious decline after 4 min. This result implies that the LDH matrix restrains the rapid deterioration of ICG and maintains its consistent activity. Moreover, the photothermal conversion efficiency of ICG(2%)-FA(20%)/LDH was also investigated and temperature increases from 19.8 °C to 51.0 °C, which is close to that of ICG(2%)/LDH (Fig. S6†). This indicates that the coexistence of FA does not affect the photothermal conversion performance of ICG. The photothermal conversion efficiency of pristine ICG, ICG/LDH and ICG-FA/LDH at 808 nm was also calculated according to the reported method.<sup>51</sup> ICG/LDH and ICG-FA/LDH show values as high as 58.3% and 56.1%, respectively, which enhance 13.6% and 11.4% compared with that of pristine ICG (44.7%). Subsequently, the influence of ICG(2%)-FA(20%)/LDH concentration in solution on the resulting photothermal conversion efficiency was studied. With the increase of ICG(2%)-FA(20%)/LDH concentration from 5  $\mu\text{g mL}^{-1}$  to 20  $\mu\text{g mL}^{-1}$ , an enhancement in light-to-thermal energy transformation is found (Fig. 3b). The results above demonstrate that the ICG(2%)-FA(20%)/LDH sample displays superior photothermal conversion efficiency as well as stability, which was chosen to evaluate its PTT effectiveness in the following section.

## 2.2 Study on NIR fluorescence imaging and *in vitro* PTT performance

The NIR fluorescence imaging of ICG(2%)/LDH and ICG(2%)-FA(20%)/LDH were studied by *in vitro* tests performed with KB cells. KB cells were incubated with pristine ICG, ICG(2%)/LDH and ICG(2%)-FA(20%)/LDH respectively, with the ICG concentration of 8  $\mu\text{g mL}^{-1}$  for 3 h, and the cell intake was studied by a confocal microscope. As shown in Fig. 4d-f, the

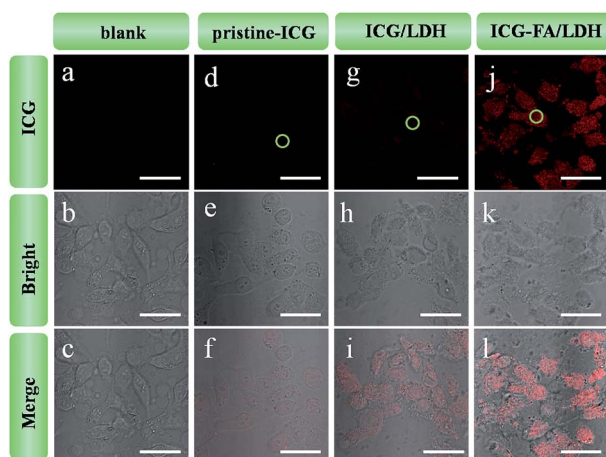


Fig. 4 *In vitro* confocal analysis images of KB cells treated with various samples (ICG concentration in solution: 8  $\mu\text{g mL}^{-1}$ , 3 h incubation): (a–c) blank, (d–f) pristine ICG, (g–i) ICG(2%)/LDH, (j–l) ICG(2%)-FA(20%)/LDH. The red fluorescence comes from ICG; the scale bar is 50  $\mu\text{m}$ .

fluorescence intensity of KB cells incubated with pristine ICG enhances slightly compared with the blank group (Fig. 4a–c), indicating a small amount of the ICG uptake. For the KB cells incubated with ICG(2%)/LDH (Fig. 4g–i), a further enhancement is observed, stronger than that of pristine ICG. The positively charged ICG/LDH nanoparticles (Fig. S4a†) are favorable for the cellular uptake with negatively charged cell membrane, accounting for its passive targeting ability. In the case of ICG(2%)-FA(20%)/LDH sample (Fig. 4j–l), the fluorescence intensity of ICG signal is significantly heightened by encapsulating targeting agent FA, which indicates the best intake performance compared with pristine ICG and ICG(2%)/LDH. Moreover, the average pixels of imaging zones can be calculated by confocal analysis software, and the fluorescence intensity of KB cells treated with ICG, ICG(2%)/LDH and ICG(2%)-FA(20%)/LDH is 3.27, 10.36 and 27.85 respectively. The fluorescence intensity for ICG(2%)-FA(20%)/LDH is 8.5-fold and 2.7-fold stronger than that of pristine ICG and ICG(2%)/LDH, exhibiting a high targeting ability of ICG(2%)-FA(20%)/LDH toward KB cells and the resulting greatly improved NIR imaging performance. Moreover, a negatively responsive cell (L-02) without folate receptor was used for a complete comparison. As shown in the confocal images (Fig. S7†), no obvious difference in the cellular uptake between KB and L-02 cell is observed when incubated with pristine ICG or ICG/LDH. However, the fluorescence intensity of KB cells incubated with ICG-FA/LDH is significantly higher than that of L-02 cells under the same conditions, demonstrating a much stronger targeting ability of ICG-FA/LDH toward KB cells.

The PTT performance of ICG-FA/LDH was further studied by *in vitro* tests performed with KB cells. To elucidate the optimized treatment conditions, two factors including NIR irradiation time and drug dosage were explored. The impact of irradiation time on PTT effectiveness was firstly investigated. The KB cells were incubated with the ICG(2%)-FA(20%)/LDH (equivalent ICG concentration: 8  $\mu\text{g mL}^{-1}$ ) for 3 h, washed thoroughly with PBS, followed by NIR irradiation ranging from 2 min to 15 min. Fig. 5a shows that the cell viability decreases sharply from 0.647 (2 min) to 0.126 (12 min), and then keeps constant upon further increasing irradiation time to 15 min, which indicates that 12 min of

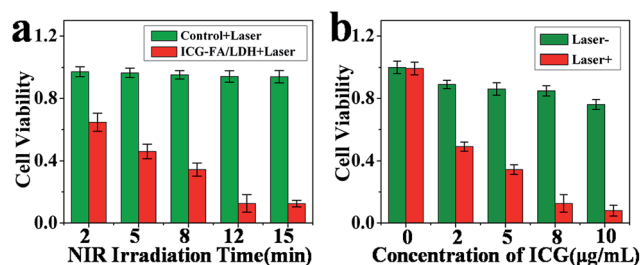


Fig. 5 (a) The PTT performance of ICG(2%)-FA(20%)/LDH along with the increase of NIR irradiation time (ICG dosage: 8  $\mu\text{g mL}^{-1}$ ); (b) the PTT performance of ICG(2%)-FA(20%)/LDH with various drug dosage upon irradiation for 12 min.

irradiation leads to a satisfactory PTT effect (808 nm; power density:  $1.1 \text{ W cm}^{-2}$ ).

Fig. 5b displays the PTT effectiveness of ICG(2%)-FA(20%)/LDH with various drug dosage under 12 min irradiation. A significant PTT effect occurs and enhances gradually along with the increase of drug dosage from 0 to  $10 \mu\text{g mL}^{-1}$ . However, an obvious cytotoxicity is observed when the concentration changes from 8 to  $10 \mu\text{g mL}^{-1}$  (cell viability without irradiation: 0.852 vs. 0.711). Therefore, the best PTT behavior is demonstrated over ICG(2%)-FA(20%)/LDH with the dosage of  $8 \mu\text{g mL}^{-1}$  for 12 min irradiation (the difference of cell viability between irradiation and no irradiation: 0.726).

For comparison, the PTT performances of pristine ICG, ICG(2%)/LDH and ICG(2%)-FA(20%)/LDH (equivalent ICG concentration:  $8 \mu\text{g mL}^{-1}$ ) were studied by incubating KB cells in these media respectively (Fig. S8-a†). The blank test shows that the irradiation imposes no influence on the cell viability. For pristine ICG, the cell viability is 0.95 (no irradiation) and 0.84 (irradiation), indicating a good biocompatibility but rather poor PTT effectiveness. For the sample of ICG(2%)/LDH, the cell viability is found to be 0.854 (no irradiation) and 0.642 (irradiation) respectively, showing a unsatisfied PTT performance ascribed to the low drug intake (Fig. 4j-i). In the case of ICG(2%)-FA(20%)/LDH, a largely-enhanced PTT effectiveness and acceptable cytotoxicity are obtained (no irradiation: 0.852; irradiation: 0.126), which can be attributed to its excellent photothermal conversion efficiency and targeted behavior *via* the over-expression of FA toward KB cells. In addition, the PTT performance of pristine FA ( $0.5 \text{ mg mL}^{-1}$ ), SDS ( $0.5 \text{ mg mL}^{-1}$ ) and LDH ( $0.5 \text{ mg mL}^{-1}$ ) was also studied (Fig. S8-b†). Both LDH and FA do not show cytotoxicity and PTT effect, demonstrating a good biocompatibility as reported previously.<sup>52-54</sup> For SDS, somewhat cytotoxicity is observed, but it is essential to achieve the dispersibility of ICG molecules in LDH matrix with the monomer state.

Visualization results were obtained by confocal analysis for KB cells, in which the live cells were stained by Calcein AM with green fluorescence and dead cells were stained by PI with red fluorescence. Fig. S9† shows the cell apoptosis treated by pristine ICG, ICG(2%)/LDH and ICG(2%)-FA(20%)/LDH with the same ICG dosage ( $8 \mu\text{g mL}^{-1}$ ) and without irradiation. Pristine ICG displays a low cytotoxicity while ICG(2%)/LDH and ICG(2%)-FA(20%)/LDH induce somewhat cell mortality. Subsequently, the PTT effectiveness of these three drugs was further investigated under NIR irradiation for 12 min (Fig. 6). The confocal image of blank group shows no obvious apoptosis for KB cells. The group of pristine ICG causes a slight apoptosis, indicating a weak PTT performance; the ICG(2%)/LDH group exhibits an enhanced apoptosis and PTT performance. In contrast, an intense PI signal is observed for the cells treated with ICG(2%)-FA(20%)/LDH, illustrating a predominant cell death after light irradiation. The results are in high accordance with the PTT tests (Fig. S8-a†), demonstrating that the ICG(2%)-FA(20%)/LDH can be used as a promising candidate in cancer NIR imaging and PTT field.

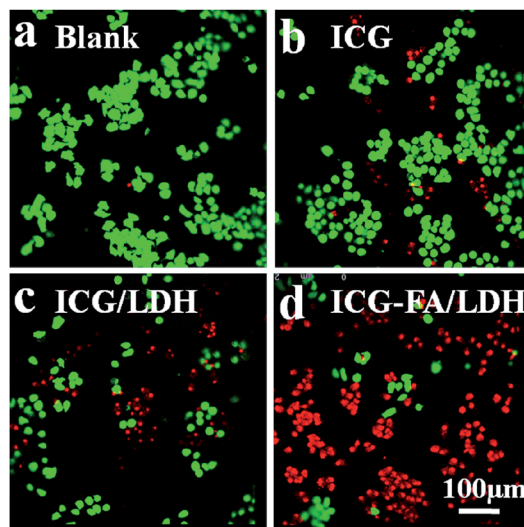


Fig. 6 Confocal fluorescence images of KB cells stained by Calcein AM/PI after treated with various drugs (equivalent ICG:  $8 \mu\text{g mL}^{-1}$ ; incubation time: 3 h) followed by an irradiation: (a) blank, (b) pristine ICG, (c) ICG(2%)/LDH, (d) ICG(2%)-FA(20%)/LDH. The scale bar is 100  $\mu\text{m}$ . The irradiation conditions: 808 nm,  $1.1 \text{ W cm}^{-2}$ , 12 min.

### 3. Conclusions

In summary, a targeted photothermal agent is synthesised by the incorporation of ICG and FA into the LDH gallery, which exhibits largely improved photothermal conversion efficiency and PTT effectiveness. The host-guest interaction between LDH matrix and ICG molecules results in the monomer state of ICG, which plays a key role in obtaining a high efficiency of photothermal conversion. *In vitro* studies with KB cells reveal that an ultra-low drug dosage of ICG(2%)-FA(20%)/LDH exhibits a satisfactory NIR imaging and PTT effectiveness with a low power of NIR irradiation ( $808 \text{ nm}$ ,  $1.1 \text{ W cm}^{-2}$  for 12 min). This is attributed to the enhanced photothermal efficiency of ICG as well as the largely elevated cellular uptake *via* the targeting capability of FA toward KB cells. In addition, the photothermal agent ICG(2%)-FA(20%)/LDH displays a good biocompatibility and improved storage stability, which would guarantee its practical application. However, the main obstacle for PTT therapy in this work originates from the illuminant penetrability and energy loss. Further studies on multimodal treatments for the purpose of synergistic therapy based on PTT and chemotherapy are under investigation in our lab.

### 4. Experimental

#### 4.1 Preparation of ICG(x%)/LDH

ICG(x%)/LDH composite nanoparticles were prepared by a coprecipitation method. Briefly, solution A:  $\text{Mg}(\text{NO}_3)_2 \cdot 6\text{H}_2\text{O}$  (0.002 mol),  $\text{Al}(\text{NO}_3)_3 \cdot 9\text{H}_2\text{O}$  (0.001 mol), sodium dodecyl sulfonate (SDS) ( $a$  mol) and ICG ( $b$  mol, in which  $a + b = 0.001$  mol;  $a : b = 99 : 1, 98 : 2, 97 : 3, 95 : 5, 90 : 10$ , respectively;  $x\% = a/(a + b)$ ) dissolved in 50 mL of methanol solution (2 : 3, v/v). Solution B: NaOH (0.006 mol) dissolved in 50 mL of deionized

water. To prevent the distraction of atmospheric CO<sub>2</sub>, distilled water was decarbonated by boiling before it was used in all the preparation processes. Solution B was added dropwisely into solution A with stirring until the pH value reached to 9. The resulting suspension was stirred at 55 °C for 40 h under a nitrogen flow. The solid product was separated by centrifuging, washed with deionized water, and dried overnight at 60 °C.

#### 4.2 Preparation of ICG(2%)-FA(20%)/LDH

The same method described above was used to synthesize ICG(2%)-FA(20%)/LDH composite material. Solution A: Mg(NO<sub>3</sub>)<sub>2</sub>·6H<sub>2</sub>O (0.002 mol), Al(NO<sub>3</sub>)<sub>3</sub>·9H<sub>2</sub>O (0.001 mol), sodium dodecyl sulfonate (SDS, 0.00098 mol), ICG (0.00002 mol) and folic acid (FA, 0.0002 mol, which was protonized by 0.001 mol mL<sup>-1</sup> NaOH before used). Solution B: NaOH (0.006 mol) dissolved in 50 mL of deionized water. Solution B was added dropwisely into solution A with stirring until pH = 9. The resulting suspension was stirred at 55 °C for 40 h under a nitrogen flow. The solid product was separated by centrifuging, washed with deionized water, and dried overnight at 60 °C.

#### 4.3 Determination of photothermal conversion efficiency

1 mL of ICG(x%)/LDH (x% = 1%, 2%, 3%, 5%, 10%) sample (ICG dosage: 10 µg mL<sup>-1</sup>) in a tube was irradiated by a NIR laser (808 nm, 1.1 W cm<sup>-2</sup>) for a period of time. The temperature was measured by a thermocouple with 30 s interval. The photothermal conversion efficiency of ICG(2%)-FA(20%)/LDH samples with different ICG concentration (5–20 µg mL<sup>-1</sup>) was determined by the same method.

#### 4.4 In vitro studies on tumor cells

KB cells were cultured and expanded in Dulbecco's modified Eagle's medium (DMEM) culture medium supplemented with 10% fetal bovine serum (FBS) and 1% penicillin-streptomycin at 37 °C under a 5% CO<sub>2</sub> atmosphere, and the cells were detached from the flask by addition of 1.0 mL of 0.25% trypsin for 1–3 min before confluence.

To study the cellular uptake of drug, KB cells or L-02 cells were seeded respectively in 96-well plates with 100 µL of medium at a density of 1 × 10<sup>4</sup> cells per well for 24 h, respectively. Pristine ICG, ICG(2%)/LDH and ICG(2%)-FA(20%)/LDH (equivalent ICG: 8 µg mL<sup>-1</sup>) were added into the wells. After a further incubation of 3 h, cells were washed with PBS for 3 times. A confocal microscopy was used to determine the drug uptake through the fluorescence intensity of ICG. ICG was excited at 633 nm with a He-Ne laser through a 633 nm long-pass filter.

To study the photothermal performance of drug, KB cells were incubated in ICG(2%)-FA(20%)/LDH (equivalent ICG: 8 µg mL<sup>-1</sup>) for 3 h, washed with PBS for 3 times, followed by an NIR irradiation (808 nm) for different time (2 min, 5 min, 8 min, 10 min, 12 min, 15 min). After a further incubation of 1 h, the colorimetric 3-(4,5-dimethylthiazol-2-yl)-2,5-diphenyltetrazolium bromide (MTT) was used to determine the cell viability. The

photothermal performance of ICG(2%)-FA(20%)/LDH (equivalent ICG: 0 µg mL<sup>-1</sup>, 2 µg mL<sup>-1</sup>, 5 µg mL<sup>-1</sup>, 8 µg mL<sup>-1</sup>, 10 µg mL<sup>-1</sup>), ICG(2%)/LDH, pristine ICG (8 µg mL<sup>-1</sup>), FA (0.5 mg mL<sup>-1</sup>), SDS (0.5 mg mL<sup>-1</sup>), LDH (0.5 mg mL<sup>-1</sup>) were performed by the same method.

KB cells were treated with DMEM (10% FBS), pristine ICG, ICG(2%)/LDH and ICG(2%)-FA(20%)/LDH (equivalent ICG: 8 µg mL<sup>-1</sup>) for 3 h respectively, followed by with or without irradiation (12 min). After washing with PBS for three times and a further incubation of 1 h, the cells were stained with propidium iodide (PI) and observed on a confocal microscope.

#### 4.5 Sample characterizations

The solid UV-vis absorption spectra were collected in the range from 200 nm to 1000 nm on a Shimadzu U-3000 spectrophotometer, with the slit width of 1.0 nm. Powder X-ray diffraction (XRD) patterns were measured on a Shimadzu XRD-6000 diffractometer in reflection mode with Cu K $\alpha$  radiation ( $\lambda$  = 0.154056 nm) under 40 kV with a scan step of 0.04°/2 $\theta$  in the range from 3 to 70°. The morphology of materials was investigated by using a scanning electron microscope (SEM, Zeiss SUPRA 55). The Fourier transform infrared (FT-IR) spectra were recorded by a Nicolet 605 XB FT-IR spectrometer in the range 4000–400 cm<sup>-1</sup> with 2 cm<sup>-1</sup> resolution. Zeta potential and dynamic lighting scattering (DLS) diameter were conducted with photon correlation spectroscopy (PCS, Nanosizer Nano ZS, MALVERN Instruments). The analysis of metal content was performed by ICP atomic emission spectroscopy (AES) on a Shimadzu ICPS-7500 instrument by dissolving the samples in dilute nitric acid. Carbon, nitrogen and sulfur analysis were carried out by a Perkin Elmer Elementarvario elemental analysis instrument. Fluorescence images were obtained using a confocal microscope (Leica TCS-SP5) with the 60 $\times$  oil-immersion objective.

## Acknowledgements

This work was supported by the 973 Program (Grant No. 2014CB932103), the National Natural Science Foundation of China (NSFC), the Innovation and Promotion Project of Beijing University of Chemical Technology and the Fundamental Research Funds for the Central Universities (YS 1406). M. Wei particularly appreciates the financial aid from the China National Funds for Distinguished Young Scientists of the NSFC.

## Notes and references

- 1 P. Huang, J. Lin, W. Li, P. Rong, Z. Wang, S. Wang, X. Wang, X. Sun, M. Aronova, G. Niu, R. D. Leapman, Z. Nie and X. Chen, *Angew. Chem., Int. Ed.*, 2013, **52**, 13958–13964.
- 2 Z. Zhou, J. Wang, W. Liu, C. Yu, B. Kong, Y. Sun and W. Wang, *Nanoscale*, 2014, **6**, 12591–12600.
- 3 E. Addae, X. Dong, E. McCoy, C. Yang, W. Chen and L. Yang, *J. Biol. Eng.*, 2014, **8**, 1–11.
- 4 Y. Ma, S. Tong, G. Bao, C. Gao and Z. Dai, *Biomaterials*, 2013, **34**, 7706–7714.

- 5 J. Xiao, S. Fan, F. Wang, L. Sun, X. Zheng and C. Yan, *Nanoscale*, 2014, **6**, 4345–4351.
- 6 S. B. Lakshmanan, X. Zou, M. Hossu, L. Ma, C. Yang and W. Chen, *J. Biomed. Nanotechnol.*, 2012, **8**, 883–890.
- 7 Y. Ma, X. Liang, S. Tong, G. Bao, Q. Ren and Z. Dai, *Adv. Funct. Mater.*, 2013, **23**, 815–822.
- 8 J. Qin, Z. Peng, B. Li, K. Ye, Y. Zhang, F. Yuan and X. Lu, *Nanoscale*, 2015, **7**, 13991–14001.
- 9 H. K. Moon, S. H. Lee and H. C. Choi, *ACS Nano*, 2009, **3**, 3707–3713.
- 10 S. Hu, Y. Chen, W. Hung, I. Chen and S. Chen, *Adv. Mater.*, 2012, **24**, 1748–1754.
- 11 F. Zhou, S. Wu, B. Wu, W. Chen and D. Xing, *Small*, 2011, **7**, 2727–2732.
- 12 Y. Li, W. Lu, Q. Huang, M. Huang, C. Li and W. Chen, *Nanomedicine*, 2010, **5**, 1161–1171.
- 13 X. Liu, Q. Ren, F. Fu, R. Zou, Q. Wang, G. Xin, Z. Xiao, X. Huang, Q. Liu and J. Hu, *Dalton Trans.*, 2015, **44**, 10343–10351.
- 14 B. Li, Q. Wang, R. Zou, X. Liu, K. Xu, W. Li and J. Hu, *Nanoscale*, 2014, **6**, 3274–3282.
- 15 Q. Chen, C. Liang, C. Wang and Z. Liu, *Adv. Mater.*, 2015, **27**, 903–910.
- 16 A. Bianco, *Angew. Chem., Int. Ed.*, 2013, **52**, 4986–4997.
- 17 X. Zheng, F. Zhou, B. Wu, W. Chen and D. Xing, *Mol. Pharm.*, 2012, **9**, 514–522.
- 18 N. Beziere, N. Lozano, A. Nunes, J. Salichs, D. Queiros, K. Kostarelos and V. Ntziachristos, *Biomaterials*, 2015, **37**, 415–424.
- 19 H. Liu, S. Pang and Y. Chan, *Journal of Plastic, Reconstructive & Aesthetic Surgery*, 2014, **67**, 231–236.
- 20 K. Yang, H. Xu, L. Cheng, C. Sun, J. Wang and Z. Liu, *Adv. Mater.*, 2012, **24**, 5586–5592.
- 21 X. Song, C. Liang, H. Gong, Q. Chen, C. Wang and Z. Liu, *Small*, 2015, **11**, 3932–3941.
- 22 M. Chen, X. Fang, S. Tang and N. Zheng, *Chem. Commun.*, 2012, **48**, 8934–8936.
- 23 L. Cheng, K. Yang, Q. Chen and Z. Liu, *ACS Nano*, 2012, **6**, 5605–5613.
- 24 J. Ge, Q. Jia, W. Liu, L. Guo, Q. Liu, M. Lan, H. Zhang, X. Meng and P. Wang, *Adv. Mater.*, 2015, **27**, 4169–4177.
- 25 Y. Liu, K. Ai, J. Liu, M. Deng, Y. He and L. Lu, *Adv. Mater.*, 2013, **25**, 1353–1359.
- 26 D. Zhang, M. Wu, Y. Zeng, L. Wu, Q. Wang, X. Han, X. Liu and J. Liu, *ACS Appl. Mater. Interfaces*, 2015, **7**, 8176–8187.
- 27 A. Hannah, G. Luke, K. Wilson, K. Homan and S. Emelianov, *ACS Nano*, 2014, **8**, 250–259.
- 28 H. Wang, C. Liu, X. Gong, D. Hu, R. Lin, Z. Sheng, C. Zheng, M. Yan, J. Chen, L. Cai and L. Song, *Nanoscale*, 2014, **6**, 14270–14279.
- 29 M. Ogawa, N. Kosaka, P. L. Choyke and H. Kobayashi, *Cancer Res.*, 2009, **69**, 1268–1272.
- 30 K. Miki, K. Oride, S. Inoue, Y. Kuramochi, R. R. Nayak, H. Matsuoka, H. Harada, M. Hiraoka and K. Ohe, *Biomaterials*, 2010, **31**, 934–942.
- 31 Z. Sheng, D. Hu, M. Zheng, P. Zhao, H. Liu, D. Gao, P. Gong, G. Gao, P. Zhang, Y. Ma and L. Cai, *ACS Nano*, 2014, **8**, 12310–12322.
- 32 T. Desmettre, J. M. Devoisselle and S. Mordon, *Surv. Ophthalmol.*, 2000, **45**, 15–27.
- 33 M. A. Yaseen, J. Yu, M. S. Wong and B. Anvari, *Biotechnol. Prog.*, 2007, **23**, 1431–1440.
- 34 S. Yoneya, T. Saito, Y. Komatsu, I. Koyama, K. Takahashi and J. Duvoll-Young, *Invest. Ophthalmol. Visual Sci.*, 1998, **39**, 1286–1289.
- 35 N. Lozano, Z. S. Al-Ahmady, N. S. Beziere, V. Ntziachristos and K. Kostarelos, *Int. J. Pharm.*, 2015, **482**, 2–10.
- 36 S. J. Kim, P. K. Bae and B. H. Chung, *Chem. Commun.*, 2015, **51**, 107–110.
- 37 A. Schonbachler, O. Glaied, J. Huwyler, M. Frenz and U. Pielers, *J. Photochem. Photobiol., A*, 2013, **261**, 12–19.
- 38 A. J. Villaraza, D. E. Milenic and M. W. Brechbiel, *Bioconjugate Chem.*, 2010, **21**, 2305.
- 39 D. G. Evans and X. Duan, *Chem. Commun.*, 2006, **42**, 485–496.
- 40 J. Bauer, P. Behrens, M. Speckbacher and H. Langhals, *Adv. Funct. Mater.*, 2003, **13**, 241–248.
- 41 Y. Dou, S. Zhang, T. Pan, S. Xu, A. Zhou, M. Pu, H. Yan, J. Han, M. Wei, D. G. Evans and X. Duan, *Adv. Funct. Mater.*, 2015, **25**, 2243–2249.
- 42 C. Chakraborty, K. Dana and S. Malik, *J. Phys. Chem. C*, 2011, **115**, 1996–2004.
- 43 S. Xu, S. Zhang, W. Shi, F. Ning, Y. Fu and H. Yan, *RSC Adv.*, 2014, **4**, 47472–47480.
- 44 J. Bujdak and N. Iyi, *Cent. Eur. J. Chem.*, 2008, **6**, 569–574.
- 45 H. Dong, S. Rahman and Z. Xu, *Pharmaceutics*, 2014, **6**, 584–598.
- 46 P. Gunawan and R. Xu, *Chem. Mater.*, 2009, **21**, 781–783.
- 47 H. Zhang, D. Pan and X. Duan, *J. Phys. Chem. C*, 2009, **113**, 12140–12148.
- 48 A.-K. Kirchherr, A. Briel and K. Mäder, *Mol. Pharm.*, 2009, **6**, 480–491.
- 49 Y. Li, T. Wen, R. Zhao, X. Liu, T. Ji, H. Wang, X. Shi, J. Shi, J. Wei, Y. Zhao, X. Wu and G. Nie, *ACS Nano*, 2014, **8**, 11529–11542.
- 50 F. Rotermund, R. Weigand and A. Penzkofer, *Chem. Phys.*, 1997, **220**, 385–392.
- 51 D. K. Roper, W. Ahn and M. Hoepfner, *J. Phys. Chem. C*, 2007, **111**, 3636–3641.
- 52 D. Li, Y. Zhang, M. Yu, J. Guo, D. Chaudhary and C. Wang, *Biomaterials*, 2013, **34**, 7913–7922.
- 53 R. Liang, R. Tian, L. Ma, L. Zhang, Y. Hu, J. Wang, M. Wei, D. Yan, D. G. Evans and X. Duan, *Adv. Funct. Mater.*, 2014, **24**, 3144–3151.
- 54 K. Ladewig, M. Niebert, Z. Xu, P. Gray and G. Lu, *Biomaterials*, 2010, **10**, 1821–1829.